ACS APPLIED MATERIALS & INTERFACES

www.acsami.org

Research Article

Engineering 3D-Printed Strontium-Titanium Scaffold-Integrated Highly Bioactive Serum Exosomes for Critical Bone Defects by Osteogenesis and Angiogenesis

Hao Liu, Ranli Gu, Wei Li, Lijun Zeng, Yuan Zhu, Boon Chin Heng, Yunsong Liu,* and Yongsheng Zhou*

Cite This: *ACS Appl. Mater. Interfaces* 2023, 15, 27486−27501

Read Online

ACCESS | Metrics & More | Article Recommendations | Supporting Information

ABSTRACT: Currently, healing of large bone defects faces significant challenges such as a bulk of bone regeneration and revascularization on the bone defect region. Here, a "cell-free scaffold engineering" strategy that integrates strontium (Sr) and highly bioactive serum exosomes (sEXOs) inside a three-dimensional (3D)-printed titanium (Ti) scaffold (Sc) is first developed. The constructed SrTi Sc can serve as a sophisticated biomaterial platform for maintaining bone morphological characteristics of the radius during the period of critical bone defect (CBD) repair and further accelerating bone formation and fibroblastic suppression via the controlled release of Sr from the superficial layer of the scaffold. Moreover, compared with sEXO from healthy donors, the sEXO extracted from the serum of the femoral fracture rabbit model at the stage of fracture healing, named BF EXO, is robustly capable of facilitating osteogenesis and angiogenesis. In addition, the underlying therapeutic mechanism is elucidated, whereby altering miRNAs shuttled by BF EXO enables osteogenesis and angiogenesis. Further, the in vivo study revealed that the SrTi Sc + BF EXO composite dramatically accelerated bone repair via osteoconduction, osteoinduction, and revascularization in radial CBD of rabbits. This study broadens the source and biomedical potential of specifically functionalized exosomes and provides a comprehensive clinically feasible strategy for therapeutics on large bone defects.

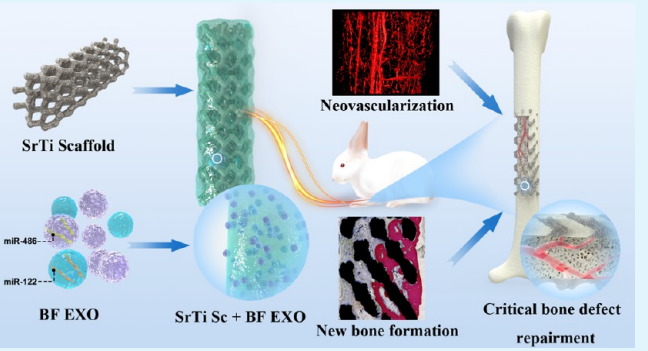

KEYWORDS: *scaffolds, strontium, exosomes, osteogenesis, angiogenesis, critical bone defect*

1. INTRODUCTION

Large bone defects resulting from tumors, trauma, infections, or congenital disorders still present a major clinical difficulty, especially at high risk of complications such as nonunion, malunion, and deep infection.[1] Poor bone regeneration and revascularization of the bone defect region are pivotal challenges, which lead to the inability of healing spontaneously for large bone defects. Clinically, large bone defects are treated by bone grafts from autologous or xenogenous, which exist with many limitations like shortage of donor sources, disease transmission, or immune rejection.[2]

Recently, a three-dimensional (3D)-printed titanium (Ti) scaffold has been increasingly applied to large bone defects to achieve customized treatment.[3] However, there are still enormous challenges to achieve satisfactory osseointegration mainly due to the immanent bio-inertness and lack of durable osteogenic ability for titanium.[4] Bone homeostasis is preserved by the balance of maintaining the activity of osteogenesis and osteoclastogenesis. Alternatively, strontium (Sr) in physiologic concentration can play a bidirectional role in promoting bone formation and inhibiting bone resorption.[5] The controlled release of Sr from the superficial layer of the scaffold is a promising clinically feasible therapeutic strategy for large bone defects.

The emerging vascular and osteoid reconstruction at the initial stage is a crucial step for bone defect healing. In recent years, exosomes have been applied for cell-free bone regeneration strategies owing to biocompatibility, low immunogenicity and cytotoxicity, and so forth.[6] To achieve excellent osteogenic ability, exosomes were obtained from osteogenic differentiation of mesenchymal stem cells (MSCs) by adding some chemical compounds in vitro, followed by treated bone defects in vivo.[7] However, the osteogenic

Received: January 24, 2023
Accepted: May 11, 2023
Published: May 22, 2023

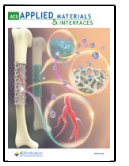

https://doi.org/10.1021/acsami.3c00898
ACS Appl. Mater. Interfaces 2023, 15, 27486−27501

Scheme 1. Based on Our "Cell-Free Scaffold Engineering" Strategy, a Composite 3D-Printed SrTi Scaffold (the First Line) was Fabricated and Highly Bioactive BF EXO (the Second Line) was Loaded into a Poloxamer-Based Hydrogel to Repair the Critical-Sized Defects of the Radius by Promoting Bone Formation, Inhibiting Bone Resorption, and Neovascularization

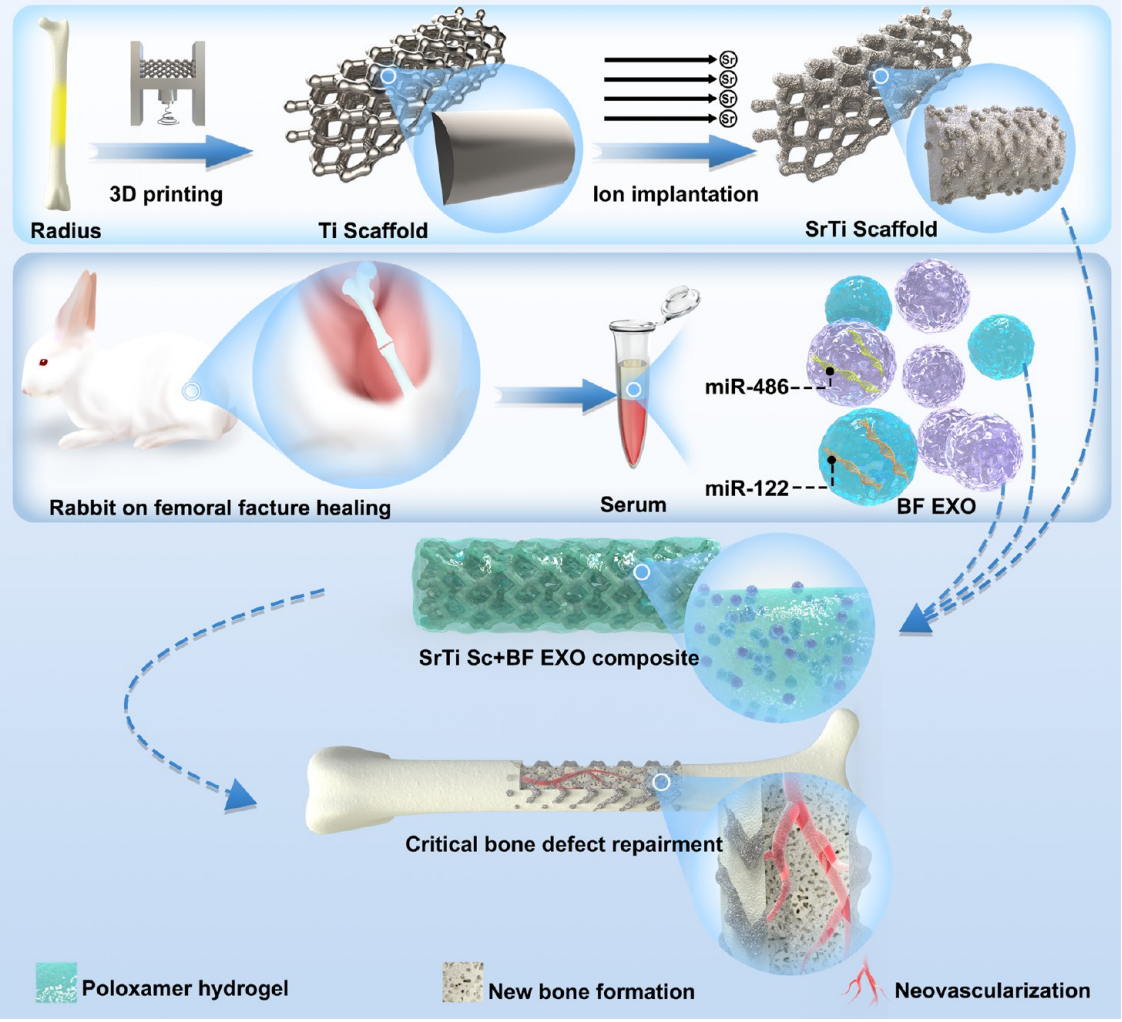

exosomes induced by chemical compounds rather than a natural osteogenic microenvironment, safety, and other possible side effects have limited its clinical translation.

Intriguingly, specifically functionalized body fluid has exhibited a promising therapeutic potential for some intractable diseases recently. For instance, Iram et. al. demonstrated that infusing young cerebrospinal fluid (CSF) directly into aged brains improved memory function because fibroblast growth factor 17 (Fgf17) from young CSF restored oligodendrocyte function in the aging brain of mice.[8] Moreover, another important research also showed that young blood exposure through heterochronic parabiosis induced stem cell revitalization and systemic rejuvenation across aged tissues of mice owing to blood-borne factors.[9] Of note, serum exosomes (sEXOs) are a kind of abundant exosomes of body fluid, which can promote angiogenesis and protect against myocardial ischemia due to carrying a large number of angiogenic factors.[10,11] However, it is insufficient to promote bone formation effectively. Clinical and preclinical studies have proven that serum during the fracture healing process contains lots of osteogenic factors including collagen X, 25(OH)D, bone morphogenetic protein-2 (BMP-2), and angiogenic factors including HIF-1α.[12−15] Therefore, sEXOs derived from the fracture repair stage (BF EXO) may contain more RNAs and proteins in angiogenesis and osteogenesis.

Poloxamers are thermo-responsive polymers, characterized by good solubilizing capacity, low toxicity, excellent drug-controlled release ability, and its compatibility with numerous biomolecules and chemical excipients. Thereinto, poloxamers 407 (P407) and 188 (P188) are widely used in drug and biomolecule administration by various routes.[16] Hence, it will be helpful for the controlled release of BF EXO in situ to design a poloxamer-based hydrogel featured by sustained release for a certain period, which could be in favor of osteogenesis and angiogenesis.

Herein, we report on a "scaffold engineering" strategy that integrates BF EXO and Sr into a 3D-printed titanium (Ti) scaffold (Sc), for critical bone defect (CBD) repairment (Scheme 1). Porous Ti Sc was printed by mimicking the radial CBD region, and Sr was injected into the superficial layer of scaffolds by ion implantation. Moreover, the bidirectional role of osteogenesis and inhibiting bone resorption of SrTi Sc were evaluated. Besides, the osteogenic and angiogenic abilities of BF EXO extracted from the serum of a femoral fracture rabbit model at the fracture healing stage were evaluated, followed by RNA sequencing and bioinformation analysis. Furthermore,

https://doi.org/10.1021/acsami.3c00898
ACS Appl. Mater. Interfaces 2023, 15, 27486−27501

SrTi Sc+BF EXO composites were implanted into the radial CBDs of rabbits to explore both osteogenesis and vascularization in vivo. Our study broadens the source and biomedical potential of specifically functionalized exosomes and provides a comprehensive, clinically feasible strategy for large bone defect therapeutics.

2. RESULTS AND DISCUSSION

2.1. Fabrication and Characterization of SrTi Sc. As shown in Scheme 1, 3D-printed Ti Sc was successfully constructed according to the shape of the midshaft of the radius (Table 1), and Sr was implanted into the superficial layer of scaffolds subsequently. The microstructures between Ti Sc and SrTi Sc were similarly observed using a stereoscope, micro-CT, a mercury porosimeter, a N_2-BET device, and scanning electron microscopy (SEM; Figure S1 and Table 2).

Table 1. Morphology and Components of the Ti Scaffold

characteristics	parameters
shape (mm)	cylinder: Ø5 × L15 (hollow inside: Ø1.5 × L15)
pore size (μm)	700
strut diameter (μm)	450
components (weight percent)	Ti (89.41), Al (5.7), V (3.8)
particle size for printing (μm)	15−45

Table 2. Characteristics of the Ti Scaffold and the SrTi Scaffold

characteristic	Ti scaffold	SrTi scaffold
porosity (%)	64.98 ± 0.48	64.76 ± 0.26
specific surface area (m^2/g)	0.1423 ± 0.0005	0.1425 ± 0.0006
surface roughness (μm)	26.90 ± 5.69	26.74 ± 5.24

However, there were numerous but minuscule sediments attached to the Ti particles in SrTi Sc rather than Ti Sc, as observed by SEM (Figure 1a). Furthermore, 4.7% Sr (wt %) exists on the surface of SrTi Sc detected by energy-dispersive spectroscopy (EDS, Figure S1d). Besides, the results of the controlled release of Sr from SrTi Sc detected by inductively coupled plasma emission spectrometer (ICP) in vitro exhibited that Sr was quickly dissolved in PBS within 10 days, released slowly between 10 and 28 days, and separated out in a trace amount in 28−84 days, which exactly met the requirement for bone regeneration (Figure 1b).[17] In addition, the biomechanical properties of Ti Sc and SrTi Sc were significantly higher than those of the radius of rabbits. Except for Young's modulus in the compression test, there were no significant differences in biomechanical parameters between Ti Sc and SrTi Sc (Table 3). Hence, SrTi Sc exhibited good biomechanical support similar to Ti Sc.

2.2. Ability to Promote Osteogenesis and Inhibit Osteoclastogenesis of SrTi Sc In Vitro. To test whether SrTi Sc had a better bidirectional ability than Ti Sc, assays on osteogenesis and inhibiting osteoclasts were performed. Compared with Ti Sc, the leach liquor of SrTi Sc significantly enhanced the osteogenic differentiation of hBMSCs, as indicated by alkaline phosphatase (ALP)/alizarin red (ARS) (two key osteogenic markers) staining and quantification (Figure 1c,e). Moreover, the SrTi Sc group also had a significantly increased gene expression on markers of osteogenesis (*SPARC*, *ALPL*, *RUNX2*, and *SPP1*) than the Ti Sc group (Figure 1f).

Generally, stimulus-induced osteoclast formation from RAW264.7 cells was extensively used as an alternative due to the difficulties associated with isolating and culturing osteoclasts in vivo.[18] The results on tartrated-resistant acid phosphatase (TRAP) staining/quantification and immunofluorescence of osteoclast-like cells (OLCs, RANKL-induced RAW264.7 cells) showed that the leach liquor of SrTi Sc significantly lessened numbers of OLCs than that of Ti Sc (Figures 1g,i and S2). Consistent with the cytological experiment, the gene expression on markers of bone resorption (*Rank*, *Rankl*, and *Trap*) had a similar tendency (Figure 1j).

Besides, in the CCK-8 assay, compared with the Ti Sc group, the leach liquor of SrTi Sc accelerated the rate of cell proliferation of hBMSCs and slowed down that of OLCs after co-culture (Figure 1d,h). However, the L929 cell viability of the SrTi Sc group significantly decreased by 5.54% compared with that of the Ti Sc group at 72 h, which means that Sr inhibited the proliferation of fibroblasts in vitro (Figure S3). Based on the aforementioned results, Sr released from SrTi Sc kept a physiologic concentration, which had an effect on bidirectional ability rather than cytotoxicity. Hence, we constructed SrTi Sc that exhibited better ability on osteogenesis and osteoclastic suppression than Ti Sc by releasing Sr ions continuously to maintain the Sr physiologic concentration.

2.3. Characterization of BF EXO. Scheme 1 also exhibits that BF EXO was extracted from the serum of rabbits during the period of femoral fracture healing. Meanwhile, CTRL EXO was obtained from healthy rabbits as performed likewise. In accord with the characteristics of CTRL EXO, BF EXO also exhibited a spherical microvesicle structure observed under a transmission electron microscope (TEM, Figure 2a). Western blot analysis revealed that the typical exosome surface markers TSG101, CD81, and CD9 expressed on both CTRL and BF EXO (Figure S4a). Besides, the average sizes of CTRL and BF EXO were 88.84 nm and 79.26 nm, respectively. Moreover, the concentrations of CTRL and BF EXO were 1.35×10^9 and 1.42×10^9 particles/ mL serum, respectively (Figure S4b). Of note, a recent study demonstrated that the concentration of sEXO was 10^2−10^3 times higher than that of exosomes extracted from the cell culture medium through any exosome isolation method, which was consistent with our research.[19] Considering exosomes from the cell culture medium as an on-the-shelf product owing to the lower productivity and high costs, the higher yield of sEXO may be a promising source for medical application. Besides, both CTRL and BF EXO could be taken up by hBMSCs (Figure S5). Unlike the controlled release of Sr, BF EXO was gradually and continuously released from a poloxamer-based hydrogel and lasted 96 h finally, which had a profound effect on the early stage of osteogenesis and angiogenesis for CBD repairment (Figure 2b).

2.4. Ability to Promote Osteogenesis and Inhibit Osteoclastogenesis of BF EXO In Vitro. Moreover, the osteogenesis of BF EXO was significantly promoted compared with that of CTRL EXO, performed by ALP/ARS staining and quantification of osteogenesis-related genes (Figure 2c,e). Moreover, the BF EXO group also had a significantly increased gene expression on markers of osteogenesis (*SPARC*, *ALPL*, *RUNX2*, and *SPP1*) than the CTRL EXO group (Figure 2f). In contrast, the representative images of TRAP/immunofluorescence staining and quantification showed that the BF EXO

https://doi.org/10.1021/acsami.3c00898
ACS Appl. Mater. Interfaces 2023, 15, 27486−27501

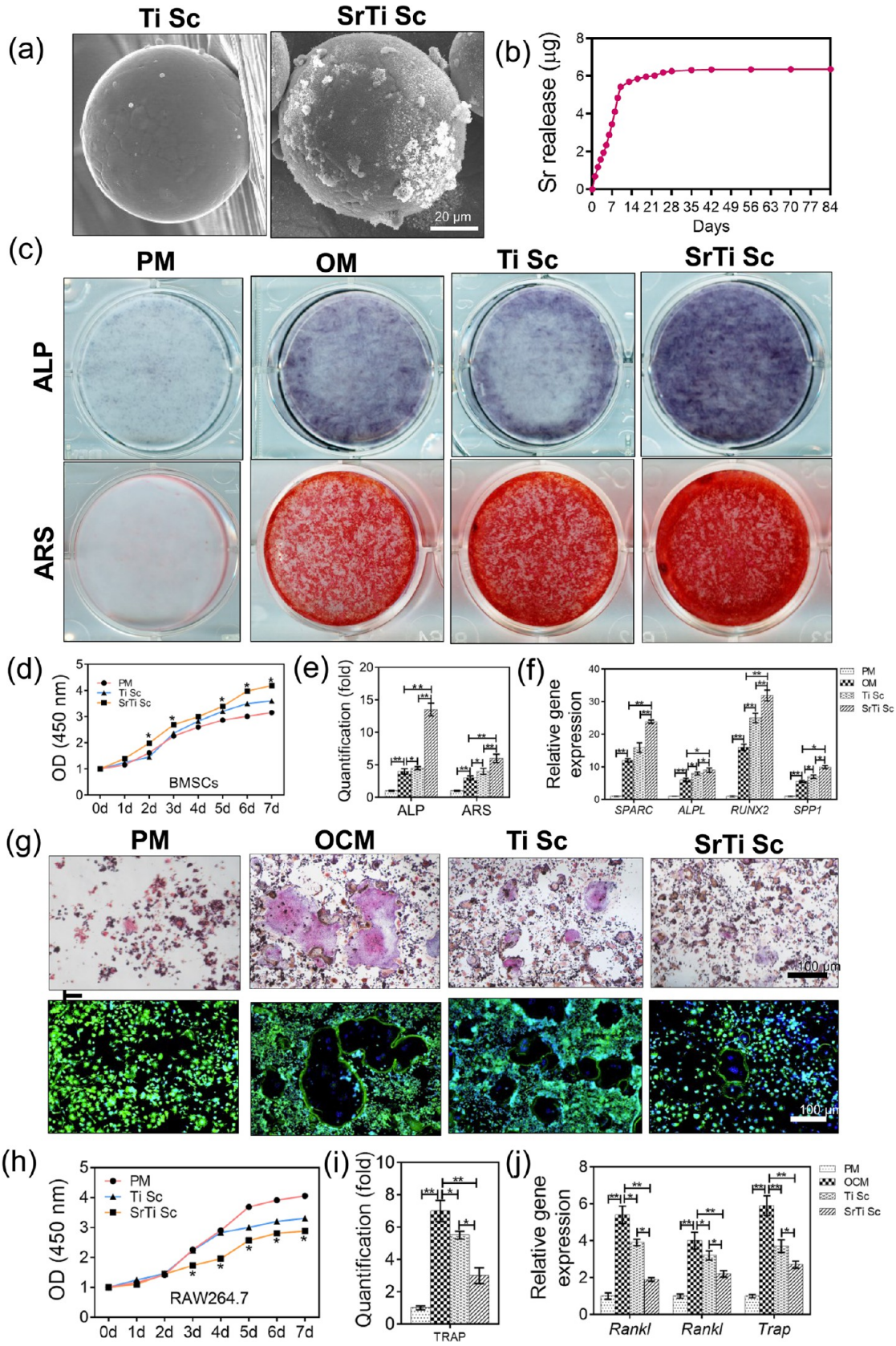

Figure 1. Ability to promote osteogenesis and inhibit osteoclastogenesis of SrTi Sc in vitro. (a) Representative images of Ti Sc and SrTi Sc detected by SEM. Scale bar = 20 μm. (b) Release curve of Sr. (c) Representative images of ALP and ARS staining. (d) Proliferation curve of hBMSCs detected by CCK-8. (e) Quantification of ALP and ARS staining. (f) Relative expression of osteogenic genes. (g) Representative images of TRAP and FITC staining. (h) Proliferation curve of RAW264.7. (i) Fold change of TRAP. (j) Relative expression of osteoclast-related genes. *P < 0.05, **P < 0.01. ALP: alkaline phosphatase; ARS: alizarin red; hBMSCs: human bone marrow-derived mesenchymal stem cells; SEM: scanning electron microscopy; TRAP: tartrate-resistant acid phosphatase.

https://doi.org/10.1021/acsami.3c00898
ACS Appl. Mater. Interfaces 2023, 15, 27486−27501

Table 3. Biomechanics among the Ti Scaffold, SrTi Scaffold, and Midshaft Radius of Rabbits

characteristic	radius of rabbit	Ti scaffold	SrTi scaffold
3-point flexural test:			
maximum load (N)	141.075 ± 22.704	1357.693 ± 124.139[a]	1452.841 ± 108.935[aa]
energy to ultimate load (mJ)	109.919 ± 47.963	672.967 ± 117.763[aa]	759.86 ± 106.103[aa]
Young's modulus (MPa)	1068.017 ± 275.661	2404.298 ± 440.434[aa]	2733.017 ± 372.079[aa]
stiffness (N/mm)	576.698 ± 163.8	3061.158 ± 564.409[aa]	3478.576 ± 489.513[aa]
compression test:			
maximum compressive load (N)	618.426 ± 66.213	2742.266 ± 137.85[aa]	2545.148 ± 218.592[aa]
compressive strength (MPa)	48.489 ± 7.367	151.543 ± 7.618[aa]	140.65 ± 12.08[aa]
Young's modulus (MPa)	3212.822 ± 454.55	7148.519 ± 473.253[aa]	6334.964 ± 291.879[a,bab]

[a]$P < 0.01$ versus the radius of rabbits. [b]$P < 0.01$ versus the Ti scaffold.

group had a lesser number of osteoclasts than the CTRL EXO group by the standard of TRAP-positive cells with more than three nuclei as osteoclasts (Figures 2g,i and S6).[20] Moreover, osteoclastogenesis-related genes including *Rank*, *Rankl*, and *Trap* in the BF EXO group were significantly downregulated than those of the CTRL EXO group (Figure 2j).

Intriguingly, BF EXO significantly enhanced the proliferation of hBMSCs and dampened the formation of OLCs compared with CTRL EXO, as shown by the CCK-8 assay (Figure 2d,h).

2.5. Migration and Angiogenic Ability of BF EXO In Vitro and In Vivo. As specifically functionalized serum exosomes with an excellent ability of bone formation, the angiogenic ability of BF EXO may also have a profound effect on CBD healing based on the mechanism of osteogenesis and angiogenesis coupling.[21] Accordingly, the effect of BF EXO on angiogenesis was evaluated by in vitro and in vivo assays using human umbilical vein endothelial cells (HUVECs). As depicted in Figure 3a,b, the rate of scratch wound closure of the BF EXO group was higher than that of the CTRL EXO group, detected by the scratch test. Furthermore, the number of migration cells in the BF EXO group was more than that in the CTRL EXO group, examined through the transwell assay (Figure 3a,c). In addition, in vitro tube formation of HUVECs on the Matrigel layer was employed to illustrate the ability of revascularization. Compared with the CTRL EXO group, the total mesh area, total segment length, and total branching length composed of HUVECs were significantly elevated in the BF EXO group (Figure 3a,d). Moreover, in vivo angiogenesis assays through subcutaneous injection of Matrigel plugs containing BF EXO/CTRL EXO or adding BF EXO/CTRL EXO into the chicken chorioallantoic membrane (CAM) exhibited that BF EXO had a better angiogenic ability than CTRL EXO (Figure 3a,e,f). Meanwhile, the results of qRT-PCR demonstrated that BF EXO significantly promoted the relative expression of angiogenic-related genes including *TGFβ*, *VEGFA*, *VEGFR-2*, and *MMP2* compared with CTRL EXO (Figure 3h). Besides, in CCK-8 assays, BF EXO treatment increased the proliferation of HUVECs compared to CTRL EXO (Figure 3g). The immunofluorescence staining and photograph of the skin of nude mice after subcutaneous injection of Matrigel plug containing CTRL EXO or BF EXO showed that there were more vein endothelial cells (VECs) in the BF EXO group (Figures 3f and S7). Taken together, characterized by relatively abundant, natural, and coupled osteogenic/angiogenic ability, BF EXO, as a key factor of the cell-free therapeutic strategy in this study, maybe played prominent roles in bone defect repairment clinically. More importantly, this study broadens the source and biomedical potential of specifically functionalized exosomes. First, the sEXO bank can be established through blood products with sophisticated management. Moreover, specifically functionalized sEXO can be classified according to indications. For instance, degenerative diseases for seniors like Alzheimer, Parkinson, osteoporosis, etc., can be tried to treat with sEXO of juniors inspired by the research on young CSF or blood.[8,9] However, extensive and deep burn wounds can be treated using sEXO from people with minor burn healing. Certainly, intractable bone trauma can be tried by BF EXO.

2.6. Mechanism for Osteogenesis and Vascularization of BF EXO. To explore the potential mechanism of BF EXO promoting both osteogenesis and vascularization, different exosome-shuttled miRNAs between BF EXO and CTRL EXO were detected by next-generation sequencing (NGS). The volcanic map of miRNA expression indicated that 59 miRNAs were upregulated, whereas 85 miRNAs were downregulated in the BF EXO group compared with the CTRL EXO group (Figure 4a). As depicted in Figure 4b, osteogenic miRNAs, such as Ocu-miR-122-5p, Ocu-miR-486-5p, Ocu-miR-93-5p, Ocu-miR-25-3p, Ocu-miR-103a-3p, Ocu-miR-142-5p, and Ocu-miR-92a-3p, were upregulated in the BF EXO group compared with the CTRL EXO group. By contrast, there were significantly downregulated miRNAs inhibiting bone formation in the BF EXO group, such as Ocu-miR-133a-3p, Ocu-miR-133b-3p, Ocu-miR-143-3p, Ocu-miR-199a-3p, Ocu-miR-27b-3p, and Ocu-miR-21-5p. Furthermore, the improved osteogenic ability of BF EXO may be involved in the RTK/Ras/MAPK pathway, BMP/Smad pathway, WNT/β-catenin pathway, and so on (Figure 4d and Table 4).[22−24]

Besides, these seven mostly upregulated miRNAs promoting angiogenesis were Ocu-miR-486-5p, Ocu-miR-93-5p, Ocu-miR-25-3p, Ocu-miR-103a-3p, Ocu-miR-142-5p, Ocu-miR-92a-3p, and Ocu-miR-142-3p in sequence. In turn, five mostly downregulated miRNAs inhibiting angiogenesis were Ocu-miR-143-3p, Ocu-miR-199a-3p, Ocu-miR-29a-3p, Ocu-miR-125b-5p, and Ocu-miR-148a-3p in sequence (Figure 4c). Furthermore, the mechanism of these miRNAs on elevated angiogenesis may be associated with the PI3K/AKT/STAT3 pathway, CCND2 pathway, IFG/VEGF pathway, and so forth (Figure 4d and Table 5).[36−38] NGS analysis demonstrated that BF EXO accelerated osteogenesis and angiogenesis through multi-target interaction among miRNAs probably, which avoided off-target effects of the single target through boosting one kind of miRNAs shuttled by exosomes.[39]

Further, mostly up/downregulated miRNAs promoting osteogenesis or angiogenesis detected by NGS were verified by *q*RT-PCR. The results on *q*RT-PCR exhibited that the

https://doi.org/10.1021/acsami.3c00898
ACS Appl. Mater. Interfaces 2023, 15, 27486−27501

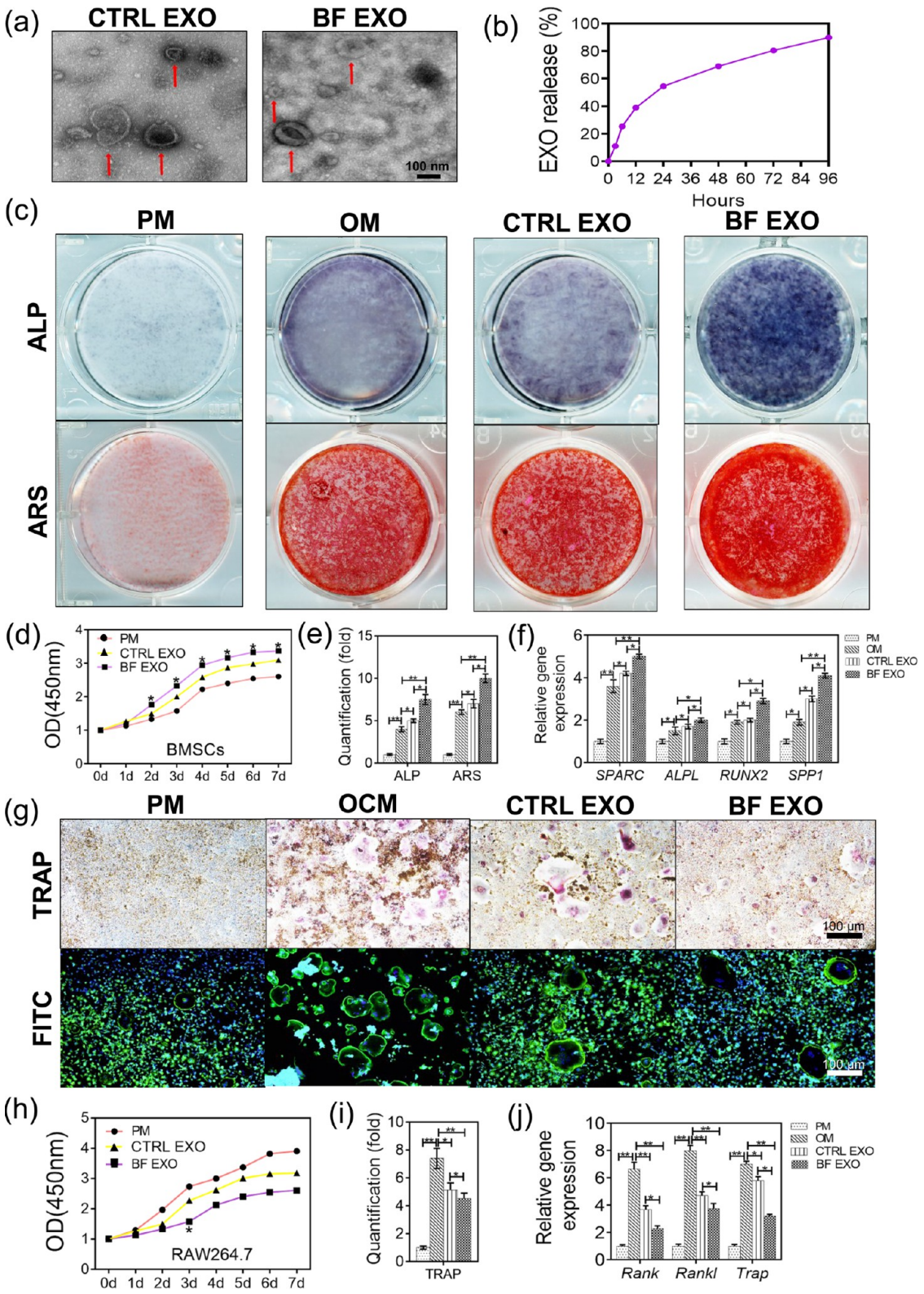

Figure 2. BF EXO enhanced osteogenesis and inhibited osteoclastogenesis in vitro. (a) Morphology of CTRL EXO and BF EXO visualized under a TEM. The red arrows indicate exosomes. Scale bar = 100 nm. (b) EXO cumulative release curve from a poloxamer-based hydrogel in vitro. (c) Representative images of ALP staining of hBMSCs treated with CTRL EXO or BF EXO. (d) Proliferation curve of hBMSCs detected by CCK-8. (e) Quantification of ALP and ARS staining. (f) Relative expression of osteogenic genes. (g) Representative images of TRAP and FITC staining. (h) Proliferation curve of RAW264.7. (i) Fold change of TRAP. (j) Relative expression of osteoclast-related genes. $^{*}P < 0.05$, $^{**}P < 0.01$. ALP: alkaline phosphatase; ARS: alizarin red; hBMSCs: human bone marrow-derived mesenchymal stem cells; TEM: transmission electron microscope; TRAP: tartrated-resistant acid phosphatase.

https://doi.org/10.1021/acsami.3c00898
ACS Appl. Mater. Interfaces 2023, 15, 27486−27501

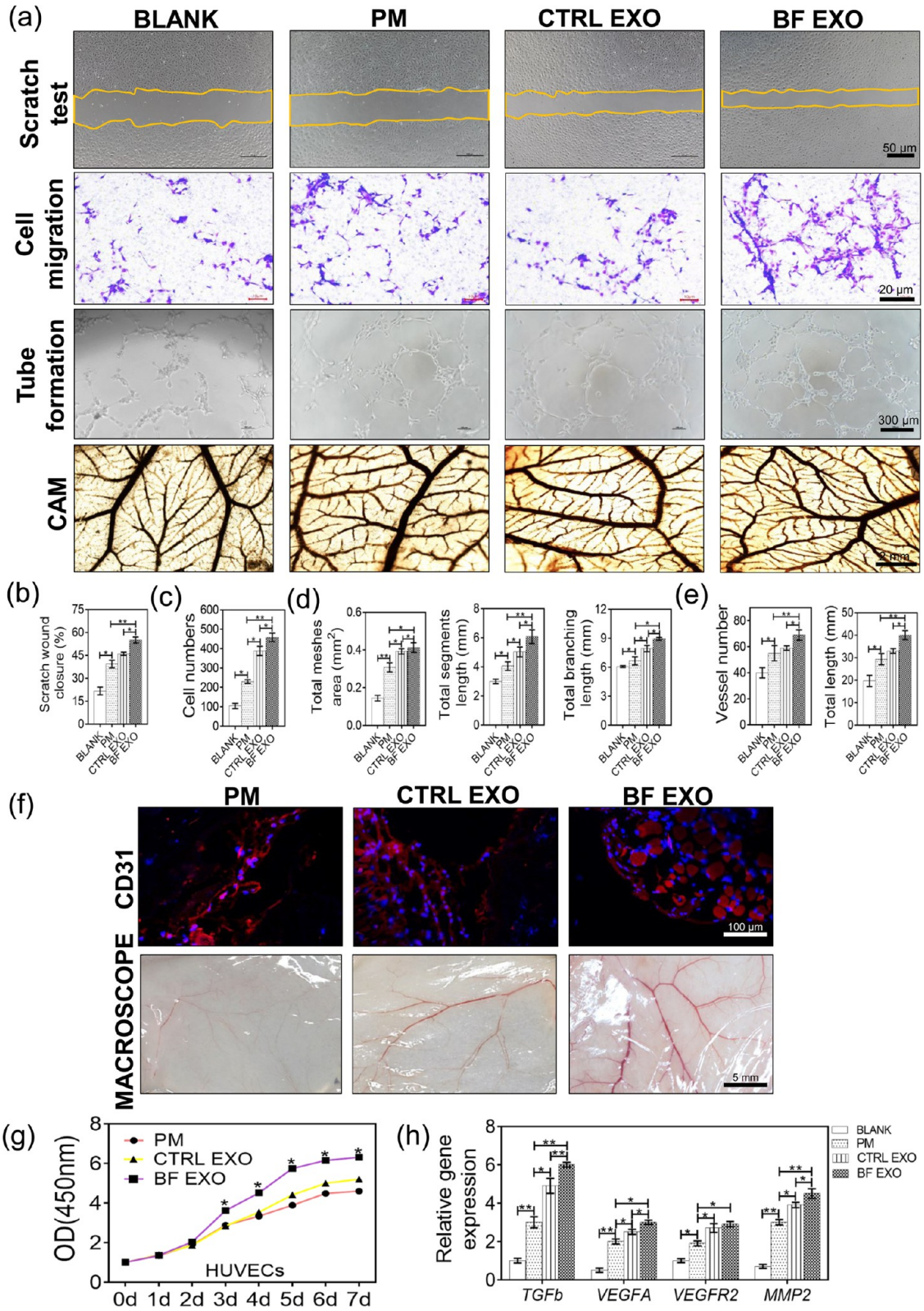

Figure 3. BF EXO significantly promoted angiogenesis both in vitro and in vivo. (a) Representative images of the scratch test, transwell assay, tube formation, and CAM test co-cultured HUVECs with CTRL EXO or BF EXO. Scale bar = 50, 20, 300 μm, and 2 mm, respectively. (b) Quantification of scratch wound closure in the scratch test. (c) Cell numbers of the transwell assay. (d) Tube formation quantification of the total mesh area, total segment length, and total branching lengths. (e) Vessel numbers and total length of CAM. (f) Representative images of immunofluorescence staining and the photograph of the skin of nude mice after subcutaneous injection of Matrigel plug containing CTRL EXO or BF EXO for 7 days. These sections were stained by the anti-mouse CD31 antibody (red) and Hoechst 33,342 (blue) to visualize VECs and cell nuclei, respectively. Scale bar = 100 μm and 5 mm, respectively. (g) Proliferation curve of HUVECs. (h) Relative expression of angiogenesis-related genes. *P < 0.05, **P < 0.01. CAM: chicken embryo chorioallantoic membrane; HUVECs: human umbilical vein endothelial cells; VECs: vein endothelial cells.

https://doi.org/10.1021/acsami.3c00898
ACS Appl. Mater. Interfaces 2023, 15, 27486−27501

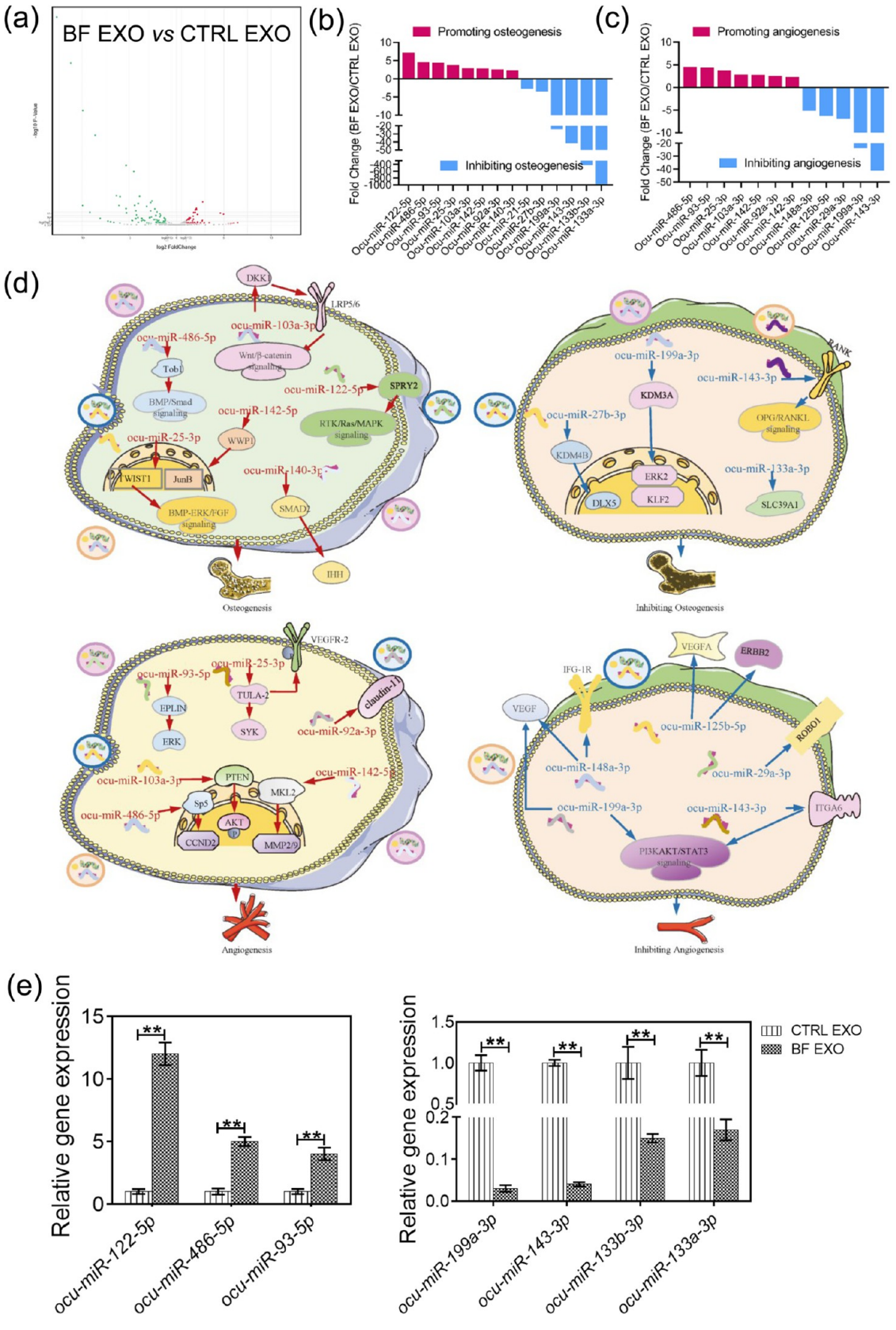

Figure 4. Potential pro-osteogenic and pro-angiogenic mechanisms of BF EXO, as detected by the NGS. (a) Volcanic map of the miRNA expression of BF EXO versus CTRL EXO. (b) Concrete miRNAs that contributed to the most significant differences in osteogenesis between BF EXO and CTRL EXO. (c) Concrete miRNAs that contributed to the most significant differences in angiogenesis between BF EXO and CTRL EXO. (d) Potential mechanism of miRNAs targeting osteogenesis and angiogenesis. NGS: next-generation sequencing. (e) Mostly up/downregulated miRNAs promoting osteogenesis or angiogenesis detected by NGS were verified by qRT-PCR.

https://doi.org/10.1021/acsami.3c00898
ACS Appl. Mater. Interfaces 2023, 15, 27486−27501

Table 4. Differentially Expressed miRNAs between BF EXO and CTRL EXO and the Potential Osteogenesis Mechanism as Reported in the Literature

miRNA	up/down	fold change	previously reported mechanisms	refs
ocu-miR-122-5p	up	6.8	activates the RTK/Ras/MAPK pathway[aa]	22
ocu-miR-486-5p	up	4.3	activates the BMP/Smad pathway[bb]	23
ocu-miR-93-5p	up	4.1	targets TCF4[cc]	25
ocu-miR-25-3p	up	3.5	activates the BMP-ERK/FGF pathway[dd]	26
ocu-miR-103a-3p	up	2.6	activates the WNT/β-catenin pathway	24
ocu-miR-142-5p	up	2.5	inhibits WWP1 and upregulates JunB[ee]	27
ocu-miR-92a-3p	up	2.3	inhibits NFκB and MAPK[ff]	28
ocu-miR-140-3p	up	2.0	inhibits Smad2 and upregulates IHH[gg]	29
ocu-miR-133a-3p	down	959	targets SLC39A1[hh]	30
ocu-miR-133b-3p	down	390	targets Mcl-1[ii]	31
ocu-miR-143-3p	down	40	activates the OPG-RANKL pathway[jj]	32
ocu-miR-199a-3p	down	22.9	targets KDM3A[kk]	33
ocu-miR-27b-3p	down	3.4	targets KDM4B[ll]	34
ocu-miR-21-5p	down	3.2	targets GDF5[mm]	35

[a]RTK/Ras/MAPK pathway: receptor tyrosine kinase/Ras/mitogen-activated protein kinase pathway. [b]BMP/Smad pathway: bone morphogenetic proteins/Smad pathway. [c]TCF4: T cell factor 4. [d]BMP-ERK/FGF pathway: bone morphogenetic proteins/extracellular regulated protein kinases/epidermal growth factor pathway. [e]WWP1: WW domain containing E3 ubiquitin protein ligase 1; JunB: Jun B proto-oncogene. [f]NFκB: nuclear factor kappa B; MAPK: mitogen-activated protein kinase. [g]IHH: Indian hedgehog homolog. [h]SLC39A1: solute carrier family 39 (zinc transporter), member 1. [i]Mcl-1: cell leukemia myeloid 1. [j]OPG-RANKL pathway: osteoprotegerin/receptor activator for the nuclear factor kappa B ligand. [k]KDM3A: lysine (K)-specific demethylase 3A. [l]KDM4B: lysine (K)-specific demethylase 4B. [m]GDF5: growth differentiation factor 5.

Table 5. Differentially Expressed miRNAs between BF EXO and CTRL EXO and the Potential Angiogenesis Mechanism as Reported in the Literature

miRNA	up/down	fold change	previously reported mechanisms	refs
ocu-miR-486-5p	up	4.3	upregulates CCND2[aa]	37, 40
ocu-miR-93-5p	up	4.1	downregulates EPLIN[bb]	41
ocu-miR-25-3p	up	3.5	upregulates SYK and VEGFR-2[cc]	42
ocu-miR-103a-3p	up	2.6	upregulates AKT[dd]	43
ocu-miR-142-5p	up	2.5	upregulates MMP2[ee]	44
ocu-miR-92a-3p	up	2.3	inhibits claudin-11	45
ocu-miR-143-3p	down	40	targets ITGA6 and activates the PI3K/AKT/STAT3 pathway[ff]	36
ocu-miR-199a-3p	down	22.9	targets VEGF[gg] and activates the PI3K/AKT/STAT3 pathway	46
ocu-miR-29a-3p	down	6.7	targets ROBO1[hh]	47
ocu-miR-125b-5p	down	6.0	upregulates ERBB2[ii] and VEGF	48
ocu-miR-148a-3p	down	4.9	upregulates IFG-1R[jj] and VEGF	38

[a]CCND2: cyclin D2. [b]EPLIN: epithelial protein lost in the neoplasm. [c]SYK: spleen-associated tyrosine kinase; VEGFR-2: vascular endothelial growth factor receptor 2. [d]AKT: serine/threonine kinase. [e]MMP2: matrix metalloproteinase 2. [f]ITGA6: integrin α6; PI3K/AKT/STAT3 pathway: phosphatidylinositol 3 kinase/AKT/signal transducer and activator of transcription 3. [g]VEGF: vascular endothelial growth factor. [h]ROBO1: roundabout guidance receptor 1. [i]ERBB2: tyrosine kinase receptor 2. [j]IFG-1R: insulin-like growth factor 1.

relative expressions of Ocu-miR-122-5p, Ocu-miR-486-5p, and Ocu-miR-93-5p had a significant increase in the BF EXO group than those in the CTRL EXO group. However, compared with the CTRL EXO group, there were a significant decrease of the relative expression of Ocu-miR-199a-3p, Ocu-miR-143-3p, Ocu-miR-133b-3p, and Ocu-miR-133a-3p in the BF EXO group (Figure 4e).

2.7. Bone Formation Ability of SrTi Sc + EXO Composites In Vivo. Encouraged by the aforementioned results, the composite was fabricated using SrTi Sc and BF EXO loaded in a poloxamer-based hydrogel and scanned by a TEM, which is depicted in Figure 5a. Immediately, SrTi Sc + EXO composites were implanted into 1.5 cm radial CBDs of rabbits (Figure 5b). Procollagen type I N-terminal propeptide (P1NP) and C-terminal telopeptide fragments of type I collagen (CTX-1) were the serum markers of bone formation and bone resorption, respectively.[49] Hence, we performed the ELISA on P1NP and CTX-1 at 3, 6, 9, and 12 weeks. Generally, the P1NP levels in the serum of the SrTi Sc + EXO group increased compared with those of the SrTi Sc or EXO group at different time points (Figure 6e). As expected, the CTX-1 levels in the serum of the SrTi Sc and SrTi Sc + EXO group were suppressed compared with the EXO group at 3 and 6 weeks. However, the inhibiting effects on CTX-1 were not obvious in the SrTi Sc + EXO group compared with the EXO group at 9 and 12 weeks, which may be due to the end of sustainedly released Sr from the SrTi Sc + EXO composite.

Furthermore, general observation, micro-CT, and undecalcified bone slicing (stained with methylene blue and fuchsin acid) were employed to evaluate bone regeneration at 6 and 12 weeks after surgery in vivo (Figure S8). At 6 weeks, there was a number of poromas surrounding the cubitus due to radial trauma in BLANK and EXO groups, whereas little bone formation existed in the region of CBD. However, in SrTi Sc and SrTi Sc + EXO groups, new bone formation induced by osteoconduction and osteoinduction existed inside and in the surrounding of the scaffolds, which provided an explanation that spatial support by scaffold and fibroblast suppression by Sr is essential to avoid connective tissue invading the region of bone formation quickly for large bone defect repair (Figure 5c,d, left column). Consistent with the respective images from micro-CT, Figure 5e exhibits that the SrTi Sc + EXO composite had significantly increased bone mineral density (BMD), bone mineral content (BMC), bone volume/total volume (BV/TV), trabecular thickness (Tb.Th), and trabecular number (Tb.N) in the CBDs of the radius compared with the Sri Sc or EXO group at 6 weeks.

At 12 weeks, the poromas surrounding the cubitus further decreased and the region of CBDs was mostly fulfilled by connective tissue in BLANK and EXO groups compared with those at 6 weeks owing to the malunion of the radius. Meanwhile, the bone regeneration outside the region of CBDs rather than inside scaffolds was further increased in the SrTi Sc

https://doi.org/10.1021/acsami.3c00898
ACS Appl. Mater. Interfaces 2023, 15, 27486−27501

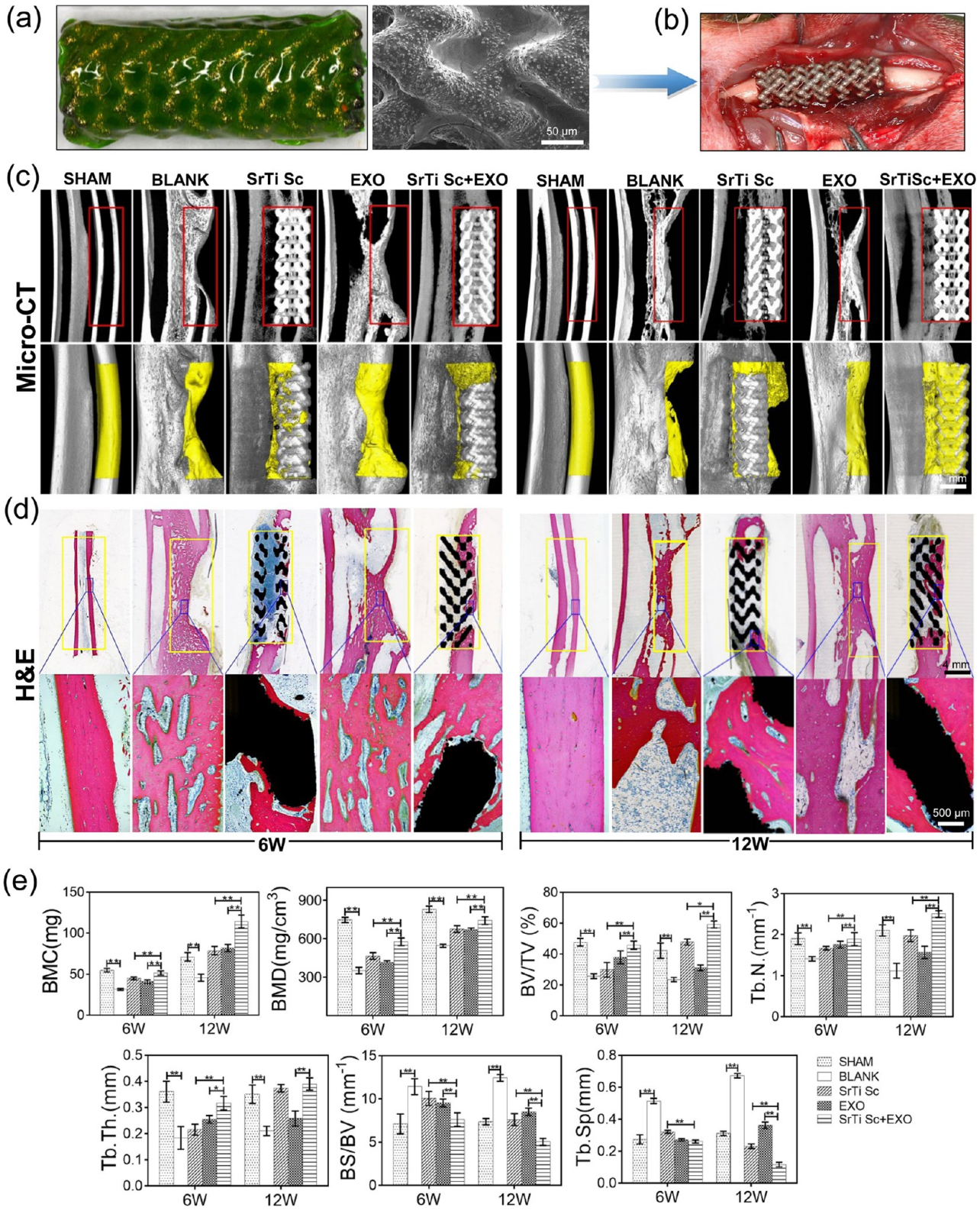

Figure 5. SrTi Sc + EXO composite scaffold promoted in vivo bone regeneration. (a) Photograph and SEM images of the SrTi Sc + EXO composite scaffold. Green represents the poloxamer-based hydrogel containing BF EXO (the transparent hydrogel was stained with calcein to improve visualization). Scale bar = 50 μm. (b) Intraoperative image of the SrTi Sc + EXO composite scaffold implanted into a critical radial defect of the rabbits. (c) Representative images of bone formation within CBDs of the radius of rabbits in each group at 6 (left) and 12 (right) weeks after surgery, as detected by micro-CT (the yellow region represents bones on CBDs of the radius of rabbits). Scale bar = 4 mm. (d) Representative images of undecalcified bone slicings of new bone formation within the CBDs of the radius of rabbits in each group (stained by methylene blue and fuchsin acid; the yellow box represents new bone formation within the CBDs of the radius of rabbits). Scale bar = 4 mm and 500 μm. (e) Bone morphometry of new bone formation within the CBDs of the radius. All statistical data are presented as mean ± standard deviation (SD; n = 5 for (B); $^*P < 0.05$, $^{**}P < 0.01$ versus SrTi Sc + EXO group). CBDs: critical bone defects.

https://doi.org/10.1021/acsami.3c00898
ACS Appl. Mater. Interfaces 2023, 15, 27486−27501

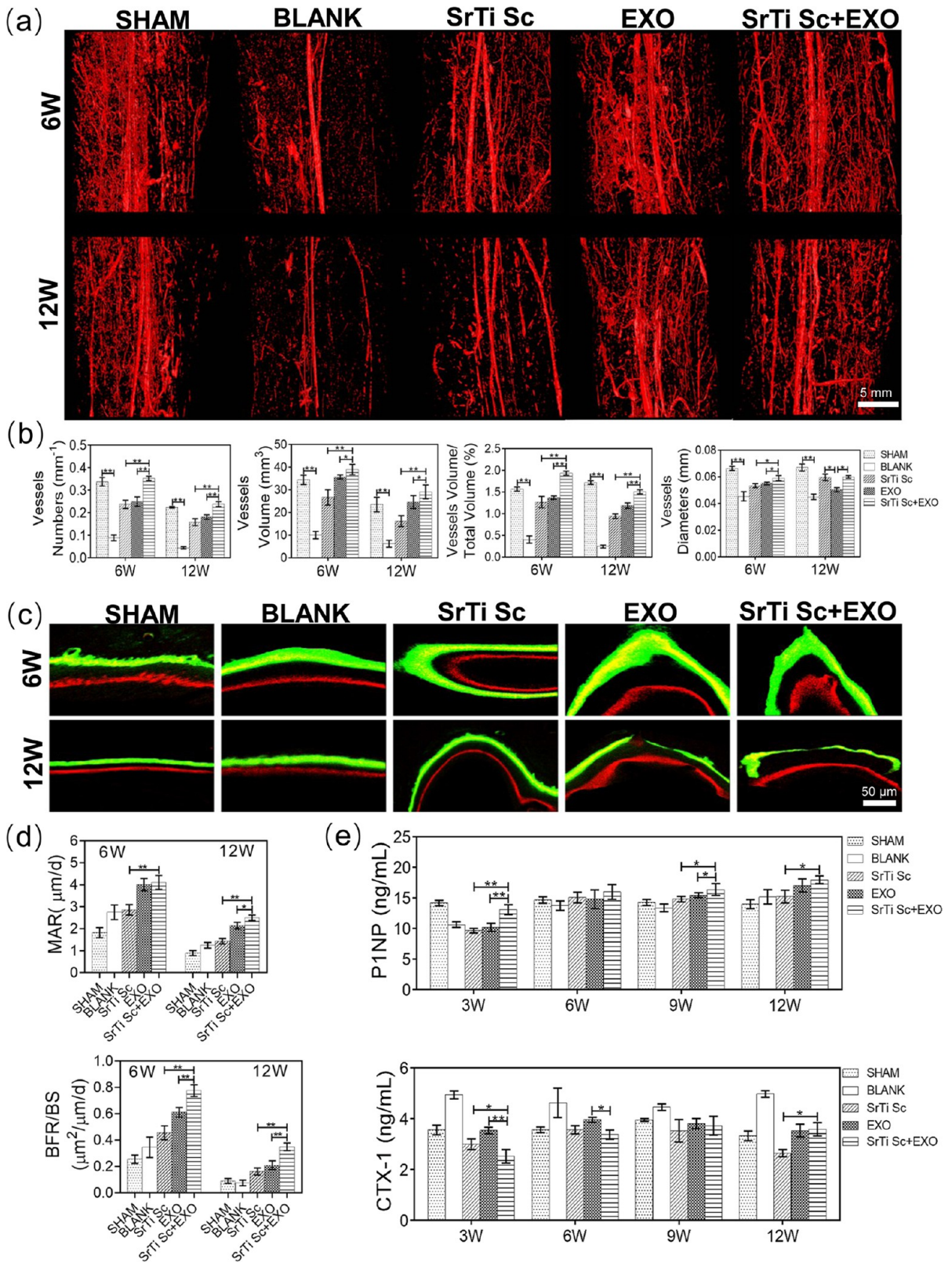

Figure 6. SrTi Sc + EXO composite scaffold promoted in vivo angiogenesis and bone regeneration. (a) Representative images of the newly formed vessels within CBDs infused by gels of high density in each group at 6 and 12 weeks post surgery, as detected by micro-CT. Scale bar = 5 mm. (b) Analysis of vessel numbers, vessel volume, vessel volume/total volume ratio, and vessel diameters at 6 and 12 weeks post surgery. (c) Representative images of double fluorescent labeling within the radial CBDs of rabbits in each group at 6 and 12 weeks post surgery. Scale bar = 50 μm. (d) Quantitative analysis of MAR and BFR/BS by double fluorescent labeling within the radial CBDs of rabbits in each group at 6 and 12 weeks post surgery. (e) Serum levels of the osteogenic marker of P1NP and CTX-1 in rabbits at 3, 6, 9, and 12 weeks post surgery. CTX-1: C-terminal telopeptide fragments of type I collagen; P1NP: procollagen type I N-terminal peptide; SEM: scanning electron microscopy.

https://doi.org/10.1021/acsami.3c00898
ACS Appl. Mater. Interfaces 2023, 15, 27486−27501

group. By contrast, new bone formation continuously increased in CBDs of the SrTi Sc + EXO group (Figure 5c,d, right column). As depicted in Figure 5e, the results of micro-CT demonstrated that compared with the SrSc Ti group or EXO group, the SrTi Sc + EXO group had a significantly higher BMD, BMC, BV/TV, and Tb.N and lower BS/BV and Tb.Sp.

Accordingly, to further evaluate the dynamic bone formation at 2 weeks, calcein and alizarin-3-methyliminodiacetic acid were intravenously injected at 3 and 1 week before euthanasia, respectively. The respective images of double fluorescent labeling demonstrated that the fluorescent bands were thick and the intervals between two bands were broad at 6 weeks compared with those at 12 weeks, which indicated that bone formation at 6 weeks was generally more vibrant than that at 12 weeks (Figure 6c). Moreover, the results of dynamic histomorphometric analyses exhibited that the mineral apposition ratio (MAR) and the bone formation ratio/bone surface (BFR/BS) in the SrTi Sc + EXO group significantly increased compared with those of the SrTi Sc or EXO group at 6 and 12 weeks (Figure 6d). Hence, the ability of bone regeneration induced by osteoconduction and osteoinduction using the SrTi Sc + EXO composite was better than that when only one was administrated.

2.8. Revascularization Ability of SrTi Sc + EXO Composites In Vivo. Furthermore, to evaluate the ability of revascularization in CBDs, gels of high density were infused into the vessels of CBDs, and the newly formed vessels of CBDs were scanned by micro-CT. Generally, at 6 and 12 weeks, the SrTi Sc + EXO and SHAM groups exhibited the most vessels among the five groups. However, there were the least vessels in the BLANK group. Besides, the vessels of SrTi Sc and EXO groups were intermediate (Figure 6a). The data calculated by micro-CT showed that SrTi Sc + EXO significantly increased the vessel number, vessel volume, vessel volume/total volume, and vessel diameter at 6 and 12 weeks compared with those of the SrTi Sc or EXO group (Figure 6b).

In this study, according to the life span of rabbits (8 years) and humans (70 years), the blood is collected at 1.5, 3.5, 5.5, and 7.5 months after bone fracture for humans equivalently. Hence, considering 3 months as a critical bone fracture recovery period for humans, we speculated that the exosomes from the human serum 3−7 months after bone fracture maybe have an excellent ability to repair bones. Moreover, the serum from the blood bank is safe and has a stable source based on the voluntary blood donation system in China. Of course, if the highly bioactive serum for bone repair can be collected, the blood bank needs to classify the blood more subtly by getting the medical information from voluntary blood donation. Hence, as a specifically functionalized exosome, BF EXO maybe has a good prospect for clinical application of bone defect repair. In the future, a more detailed study is still needed to be performed.

3. CONCLUSIONS

Based on the "cell-free scaffold engineering" strategy, a composite was fabricated using SrTi sc and BF EXO loaded in poloxamer-based hydrogels to repair the CBDs of the radius. The composite realized quick osteogenesis and osteoclastic suppression at an early stage by combined Sr and BF EXO release, followed by continuous osteoconduction, osteoinduction, and fibroblastic suppression through the sustained release of Sr. Furthermore, the revascularization of CBDs was improved by BF EXO to meet coupling osteogenic/angiogenic ability for CBD repairment. Moreover, these effects may be related to the regulation of multiple miRNAs shuttled by BF EXO. The therapy combining SrTi Sc and BF EXO is an effective, biocompatible, and clinically feasible strategy for large bone defect therapeutics. Meanwhile, this study broadens the source and biomedical potential of specifically functionalized exosomes like BF EXO. The sEXO bank for clinical therapy may be established owing to the relatively abundant and natural characteristics of sEXO, and specifically functionalized sEXO from the sEXO bank can be further classified according to indications.

4. EXPERIMENTAL SECTION

4.1. SrTi Scaffold Fabrication. For fabricating the Ti scaffold, 3D printing using the selective laser melting (SLM) method was performed. First, the radius of rabbits was scanned by micro-CT. Next, the standard triangulation language (STL) file on critical bone defects (CBDs) of the radius was generated and input to the EBM S12 system (Arcam AB, Sweden). Meanwhile, medical-grade Ti_6Al_4V powder (particle size 15−45 μm) was purchased from AP&C Company (Quebec, Canada), melted layer by layer, and further solidified by cooling to generate 3D Ti Sc. Finally, Ti Sc was ultrasonically cleaned and constructed successfully.

Then, Sr was sputtered into a superficial layer of Ti Sc by ion implantation using an industrial PVD system (CemeCon AG, Germany). The implantation energy was 60 keV and the retained dose of Sr was 1×10^{17} ions/cm^2. After that, the SrTi scaffold was fabricated successfully.

4.2. Characterization for Scaffolds. A picture of the microstructure of scaffolds was taken by a camera, and the morphology was scanned by a scanning electron microscope (Hitachi, Japan). The surface chemical composition was recorded by EDS. The porosity was detected using a mercury porosimeter (Quantachrome Instruments). The specific surface area was tested using the N_2-BET method and the 3D surface roughness was characterized through micro-CT. The mechanical strength (3-point flexural test and compression test) was detected by a mechanical testing system (MTS Inc.).

4.3. Serum Exosome (sEXO) Extraction. All animal experiments were approved by the Animal Care and Use Committee of Peking University Health Science Center (approval number: LA2019018; Beijing, China). Twenty male New Zealand white rabbits (25 weeks, 3.5 ± 0.3 kg) were purchased from Vital River Inc. (Beijing, China) and randomly grouped as the CTRL (control) group and the BF (bone fracture) group.

In order to extract exosomes from the fracture healing period, we first constructed a rabbit femoral fracture model according to the previously described methodology.[50] Briefly, the rabbits were anesthetized using pentobarbital sodium (30 mg/kg), the left femurs were fractured by rongeur forceps, and a 4 cm intramedullary nail (RabbitNail, RISystem, Switzerland) was introduced and locked in the fractured left femur. Venous blood samples were collected up to 20 mL from the rabbits of the CTRL or BF group on the 5th day after femoral fracture, once every week, a total of four times. Based on the life span of rabbits (8 years) and humans (70 years), the blood was collected on the 44th, 105th, 166th, and 227th day (approximately equivalent to 1.5, 3.5, 5.5, and 7.5 months, respectively) after bone fracture for humans equivalently.

sEXO was extracted by methods of ultracentrifugation. Briefly, serum was centrifuged at 3000 rpm for 10 min. After that, the cells and cell debris were removed by centrifugation at 2000g for 20 min followed by second centrifugation at 10,000g for 30 min. Next, the supernatant was ultracentrifuged (Beckman) at 100,000g for 80 min. The pellet was washed with PBS and centrifuged at 100,000g for another 80 min.

4.4. Characterization for sEXO. The morphology of sEXO was observed by a TEM (Hitachi, Japan). The concentration and particle size of sEXO were measured by a NanoSight NS300 (Malvern, U.K.).

https://doi.org/10.1021/acsami.3c00898
ACS Appl. Mater. Interfaces 2023, 15, 27486−27501

The typical exosome surface markers on TSG101, CD81, and CD9 were detected by WB analysis (CST).

4.5. Preparation of the Poloxamer-Based Hydrogel. The poloxamer-based hydrogels were obtained according to the previous description.[51] Briefly, poloxamers 407 and 188 (BASF, Germany) and sodium chloride (Xiya Reagent Co., Ltd, Linyi, China) were added to distilled water with stirring at 4 °C; the final components are shown in Table 6. The gels completely dissolved overnight at 4 °C. sEXO was added to poloxamer-based hydrogels at a concentration of 1.4×10^{11} particles/mL (the amount of sEXO from about 100 mL of serum of rabbits/mL hydrogels).

Table 6. Components of the Poloxamer-Based Hydrogel

material	components (wt %)
poloxamer-based hydrogel	poloxamer 407 (15), poloxamer 188 (20), NaCl (2), H_2O (63)

4.6. Sr Ion and sEXO Release Testing. SrTi Sc was immersed in SBF buffer at 37 °C. Little aliquots were removed and fresh SBF buffer were supplemented subsequently. The concentration of Sr was detected by an ICP (PerkinElmer). Besides, the sEXO cumulative release was detected by the above-mentioned methods. The concentration of sEXO was determined by a NanoSight NS300.

4.7. Cell Culture, Cell Proliferation, and Cell Uptake Assays. L929 cells, hBMSCs, HUVECs, and RAW264.7 cells were purchased from ScienCell Research Laboratories (California). Among these cells, L929 cells were selected for the cytotoxicity of scaffolds. hBMSCs were selected for detecting osteogenesis and RAW264.7 cells were selected for detecting osteoclastogenesis. HUVECs were used for examining angiogenesis. hBMSCs and RAW264.7 cells were cultured in α-MEM (Gibco BRL/Invitrogen, Carlsbad) supplemented with 10% FBS (Hyclone). HUVECs and L929 cells were cultured in DMEM supplemented with 10% FBS and antibiotics (Sigma). All cells were cultured at 37°C containing 5% CO_2.

CCK-8 (Dojindo Laboratories, Japan) was used to measure the cell proliferation ratio according to the manufacturer's instructions. The exosomes were stained by DIL (red, Beyotime Bio, China) and hBMSCs were stained by FITC (green) and DAPI (blue) (Abcam, U.K.). After that, CTRL EXO or BF EXO was co-cultured with hBMSCs for 6 h. The samples were observed using a confocal fluorescence microscope (Olympus, Japan).

4.8. Immunofluorescence Staining. Cells or nude mouse skins were fixed with 4% paraformaldehyde for 10 min. Then, the samples were treated with 0.2% Triton X-100 for 20 min and washed with PBS at 37 °C for 30 min. For nude mouse skins, primary antibodies against CD31 (1:1000; Abcam) were incubated at 4 °C overnight. For RAW264.7 cells, goat anti-rabbit FITC (1:1000; CST) was incubated at 37 °C for 30 min. After that, the cellular nuclei were counterstained with DAPI. After staining, the samples were observed using a confocal fluorescence microscope (Olympus, Japan).

4.9. Alkaline Phosphatase (ALP) Detection and Alizarin Red S (ARS) Staining. For osteoinduction assays, 10 mM β-glycerophosphate, 10 nM dexamethasone, and 50 μg/mL L-ascorbic acid were added to the maintenance medium (GIBCO). hBMSCs were seeded at 40,000 cells/well in 6-well plates. Next, CTRL EXO or BF EXO was added to the culture medium at a concentration of 7×10^9 particles/mL (amount of sEXO from about 5 mL of serum of rabbits/mL). For ALP activity, the cells were then stained with an NBT/BCIP staining kit (CoWin Biotech, China) after osteoinduction for 7 days. Besides, the cells were stained with a 2% Alizarin red S staining solution (Sigma) for ARS staining after osteoinduction for 14 days.

4.10. Tartrate-Resistant Acid Phosphatase (TRAP) Staining. RAW264.7 cells were seeded in 48-well plates. RANKL (50 ng/mL, Abcam, Cambridge, U.K.) was added after 24 h for osteoclast induction of RAW264.7 cells for 4 days. Osteoclastic differentiation of RAW264.7 cells was evaluated by TRAP staining (Sigma) and the TRAP activity assay (Takara, Japan) according to the manufacturer's instructions.

4.11. Real-Time PCR. Total RNA was extracted by TRIzol reagent (Invitrogen), and first-strand cDNA was then synthesized using a Prime Script RT Reagent Kit (Takara, Japan). After that, *q*RT-PCR was performed using a 7500 Real-Time PCR Detection System (Applied Biosystems). The following thermal settings were used: 95 °C for 10 min, followed by 40 cycles of 95 °C for 15 s and 60 °C for 1 min. The internal controls for mRNAs and miRNAs were GAPDH and U6, respectively. The data were analyzed using the $2^{-\Delta CT}$ relative expression method. The primers used in this study are shown in Table S1.

4.12. Scratch Test. The cells were seeded in 6-well plates. After incubation for 4−6 h in a serum-free medium, HUVECs were scraped with a 100 μL sterile micropipette tip. Next, the cells were added to CTRL EXO or BF EXO. Then, at 0, 3, and 6 h, migratory cells were recorded through a microscope (OLYMPUS, Japan) and analyzed by using Image-Pro Plus 6.0 software (Maryland).

4.13. Transwell Migration Assay. To investigate the effect of sEXO on migration of HUVECs, the transwell assay was detected. Briefly, 1×10^4 cells cultured in a serum-free medium were added to the upper chamber, and sEXOs (CTRL EXO or BF EXO) were added to the serum-free medium in the lower chamber of the transwell system (BD falcon). After that, the transwell system was incubated at 37 °C for 8 h. The cells were removed and the remaining cells on the undersurface of the transwell were fixed using 4% PFA. After staining with crystal violet, the cells were visualized under a microscope.

4.14. Tube Formation Assay. First, 10 μL of Matrigel (BD) was added to the bottom of each vasculogenic glass slide. After the Matrigel solidified, the cell suspension was added and treated with CTRL EXO or BF EXO for 24 h. The tube formation was performed by a microscope and Image-Pro Plus 6.0 software (Maryland)

4.15. Matrigel Plug Assay. 200 μL of Matrigel containing 30 IU/mL heparin (Sigma), 1 μg/mL VEGF (Sigma), and CTRL EXO or BF EXO (about 2.8×10^{10} particles) was subcutaneously injected into 8-week male nude mice. After 7 days, Matrigel plugs were excised for immunofluorescence analyses. Besides, photographs of newly formed vessels on the skins of nude mice were taken with a digital camera (Cannon, Japan).

4.16. Chicken Chorioallantoic Membrane (CAM) Assay. Fertilized chicken eggs (Dafeng Breeding Co. Ltd, Beijing, China) were used to perform the CAM assay. A window with a diameter of 1 cm was opened in the eggshell. Next, 100 μL of the primary medium (PM) with CRTL EXO or BF EXO (about 1.4×10^{10} particles) was added to the CAM and then the window was closed using a piece of sterile adhesive tape. Eggs were placed in a 37 °C incubator with 80% humidity. After 4 days, CAMs were fixed by a mixed solution (methanol/acetone = 1:1) for 15 min before it was harvested. Photographs were taken with a digital camera (Cannon, Japan).

4.17. Next-Generation Sequencing (NGS) for sEXO. The NGS (Wayen Biotechnologies, Shanghai, China) was applied to explore the miRNA expression. First, the miRNA library was constructed through the QIAseq miRNA Library Kit. Next, the raw fastq data quality was handled by Cutadapt, perl5, and Bowtie software. Furthermore, the normalization and quantification of miRNA were performed by the comparison of the miRBse database. Meanwhile, the edgeR program was used to identify the differentially expressed genes. The gene with a fold change of expression >1.5 was defined as a differentially expressed one.

4.18. Animals and Surgical Procedures. 100 adult male New Zealand white rabbits (25 weeks, 3.5 ± 0.3 kg) were purchased from Vital River Inc. (Beijing, China) and were randomly assigned to five groups (20 rabbits for each group): (1) CTRL group (healthy rabbits); (2) BLANK group (rabbits of radial defects without any treatment); (3) SrTi Sc group (rabbits of radial defects treated with implantation of the SrTi scaffold); (4) EXO group (rabbits of radial defects treated with BF EXO loaded in poloxamer-based hydrogels); (5) SrTi Sc + EXO group (rabbits of radial defects treated with the composite on the SrTi scaffold and BF EXO loaded in poloxamer-based hydrogels). First, a rabbit large bone defect model was performed according to standard procedures. Briefly, rabbits in each group were anesthetized by intravenous (i.v.) injection of

https://doi.org/10.1021/acsami.3c00898
ACS Appl. Mater. Interfaces 2023, 15, 27486−27501

pentobarbital sodium (30 mg/kg). Then, the rabbits' fur was excised from the front limb to expose the radius. The periosteum of the bone surface was peeled off, and 1.5 cm bone defects from the left radial midshaft were performed. Meanwhile, sterile SrTi Sc was immersed into poloxamer-based hydrogels containing BF EXO on ice. Immediately, the composite or other materials as mentioned above were implanted into radius defects precisely. Finally, the periosteum, muscle, and skin were sutured in sequence and antibiotics were injected to prevent infection. No additional fixation was used.

Six weeks after surgery, 50 rabbits were randomly euthanized (10 rabbits from each group), the serum was collected, and the left radius was excised. In brief, five rabbits in each group were performed for micro-CT and subsequent undecalcified histological slices. The other five rabbits in each group were operated for vascular infusion and then analyzed by micro-CT. The scheme at 12 weeks was the same as that at 6 weeks.

4.19. Assay on Serum Biochemical Markers of Bone Turnover. To evaluate the serum biomarkers of bone turnover, the ELISAs on P1NP and CTX-1 (IDS, Germany) were performed according to the manufacturer's instructions.

4.20. Micro-CT Analysis. To explore the differences in bone masses and microarchitectures among these groups, an Inveon MM system (Siemens, Germany) of micro-CT was used to detect the specimens. Briefly, images of bone defects were scanned with a pixel size of 9.08 μm, a current of 500 μA, a voltage of 80 kV, and an exposure time of 1000 ms in each of the 360 rotational steps. 1536 slices were contained in the projection and had a voxel size of 9.08 μm. 3D visualization images were reconstructed and the parameters were calculated using Inveon Research Workplace (Siemens) as follows: BMD, BMC, BV/TV, Tb.N, BS/BV, Tb.Sp, and Tb.Th of newly formed bones; vessel volume, vessel volume/total volume, vessel numbers, and vessel diameters of newly formed vessels in the region of radial defects.

4.21. Histology. First, calcein (20 mg/kg BW, i.v.) and alizarin-3-methyliminodiacetic acid (30 mg/kg BW, i.v.) were injected into rabbits at 3 and 1 week before euthanasia, respectively. After that, the radius was fixed and embedded in methyl methacrylate resin. Next, the slicings were ground and polished to 50 μm using the EXAKT system (EXAKT Apparatebau, Germany) and stained with methylene blue and fuchsin acid. Moreover, the mineral apposition rate (MAR) and bone formation rate/bone surface (BFR/BS) were tested using Bioquant software (BioQuant).

4.22. Lead Tetroxide Infusion for Newly Formed Vessel Detection. The rabbits received heparin (1000 IU/kg, s.c., Sigma) injections. Next, the proximal inferior vena cava and artery of rabbits were ligatured, and a 24-gauge indwelling needle was cannulated into the left ventricular. Meanwhile, the right atrium was cut into a tiny slit using ophthalmic scissors. After that, approximately 200 mL of NS, 100 mL of neutral formalin, and 50 mL of high-density lead tetroxide contrast solution were infused through the circulatory system. The contrast agent was 40% Pb_3O_4 and 5% gelatin in NS. After that, the radius was dissected and fixed in 10% formalin. The samples were scanned by micro-CT, subsequently.

4.23. Statistical Analysis. All results are presented as mean ± SD and were analyzed using SPSS 17.0 software (SPSS Inc.). Comparisons between two groups were performed using an unpaired Student's *t*-test. One-way analysis of variance (ANOVA) was used for comparisons among three or more groups. $^{*}P < 0.05$ was regarded as statistically significant, and $^{**}P < 0.01$ was regarded as highly significant.

■ ASSOCIATED CONTENT

Data Availability Statement

All source data and additional results of this study are available from the corresponding author upon reasonable request.

Supporting Information

The Supporting Information is available free of charge at https://pubs.acs.org/doi/10.1021/acsami.3c00898.

Photograph and micro-CT images of SrTi Sc; representative images of immunofluorescence staining; statistical bar graph of cell viability; characterization analysis of CTRL EXO and BF EXO; and photograph of new bones on the CBDs of the radius of rabbits (PDF)

■ AUTHOR INFORMATION

Corresponding Authors

Yunsong Liu − *Department of Prosthodontics, Peking University School and Hospital of Stomatology, Beijing 100081, China; National Clinical Research Center for Oral Diseases & National Engineering Laboratory for Digital and Material Technology of Stomatology & Beijing Key Laboratory of Digital Stomatology, Beijing 100081, China;* orcid.org/0009-0007-6498-5098; Email: liuyunsong@hsc.pku.edu.cn

Yongsheng Zhou − *Department of Prosthodontics, Peking University School and Hospital of Stomatology, Beijing 100081, China; National Clinical Research Center for Oral Diseases & National Engineering Laboratory for Digital and Material Technology of Stomatology & Beijing Key Laboratory of Digital Stomatology, Beijing 100081, China;* orcid.org/0000-0002-4332-0878; Email: kqzhouysh@hsc.pku.edu.cn

Authors

Hao Liu − *The Central Laboratory, Peking University School and Hospital of Stomatology, Beijing 100081, China; National Clinical Research Center for Oral Diseases & National Engineering Laboratory for Digital and Material Technology of Stomatology & Beijing Key Laboratory of Digital Stomatology, Beijing 100081, China;* orcid.org/0000-0002-5181-7024

Ranli Gu − *Department of Prosthodontics, Peking University School and Hospital of Stomatology, Beijing 100081, China; National Clinical Research Center for Oral Diseases & National Engineering Laboratory for Digital and Material Technology of Stomatology & Beijing Key Laboratory of Digital Stomatology, Beijing 100081, China*

Wei Li − *Department of Oral Pathology, Peking University School and Hospital of Stomatology, Beijing 100081, China; National Clinical Research Center for Oral Diseases & National Engineering Laboratory for Digital and Material Technology of Stomatology & Beijing Key Laboratory of Digital Stomatology, Beijing 100081, China; Research Unit of Precision Pathologic Diagnosis in Tumors of the Oral and Maxillofacial Regions, Chinese Academy of Medical Sciences (2019RU034), Beijing 100081, China*

Lijun Zeng − *Department of Prosthodontics, Peking University School and Hospital of Stomatology, Beijing 100081, China; National Clinical Research Center for Oral Diseases & National Engineering Laboratory for Digital and Material Technology of Stomatology & Beijing Key Laboratory of Digital Stomatology, Beijing 100081, China*

Yuan Zhu − *Department of Prosthodontics, Peking University School and Hospital of Stomatology, Beijing 100081, China; National Clinical Research Center for Oral Diseases & National Engineering Laboratory for Digital and Material Technology of Stomatology & Beijing Key Laboratory of Digital Stomatology, Beijing 100081, China*

Boon Chin Heng − *The Central Laboratory, Peking University School and Hospital of Stomatology, Beijing 100081, China; National Clinical Research Center for Oral*

https://doi.org/10.1021/acsami.3c00898
ACS Appl. Mater. Interfaces 2023, 15, 27486−27501

Diseases & National Engineering Laboratory for Digital and Material Technology of Stomatology & Beijing Key Laboratory of Digital Stomatology, Beijing 100081, China

Complete contact information is available at: https://pubs.acs.org/10.1021/acsami.3c00898

Notes

The authors declare no competing financial interest.

The authors declare that they have no known competing financial interests or personal relationships that could have appeared to influence the work reported in this paper.

■ ACKNOWLEDGMENTS

This research was supported by the National Natural Science Foundation of China (Nos. 81930026, 82170929, and 81970908), Beijing Natural Science Foundation-Haidian Original Innovation Joint Fund Project (Nos. L222145 and L222090), Peking University Medicine Fund for Fostering Young Scholars' Scientific & Technological Innovation (No. BMU2022PY010), and the Fundamental Research Funds for the Central Universities (No. PKU2022XGK008).

■ REFERENCES

(1) Migliorini, F.; La Padula, G.; Torsiello, E.; Spiezia, F.; Oliva, F.; Maffulli, N. Strategies for large bone defect reconstruction after trauma, infections or tumour excision: a comprehensive review of the literature. *Eur. J. Med. Res.* **2021**, *26*, No. 118.

(2) Norris, B. L.; Vanderkarr, M.; Sparks, C.; Chitnis, A. S.; Ray, B.; Holy, C. E. Treatments, cost and healthcare utilization of patients with segmental bone defects. *Injury* **2021**, *52*, 2935−2940.

(3) Chen, J.; Li, S.; Jiao, Y.; Li, J.; Li, Y.; Hao, Y. L.; Zuo, Y. In Vitro Study on the Piezodynamic Therapy with a BaTiO3-Coating Titanium Scaffold under Low-Intensity Pulsed Ultrasound Stimulation. *ACS Appl. Mater. Interfaces* **2021**, *13*, 49542−49555.

(4) Chang, B.; Song, W.; Han, T.; Yan, J.; Li, F.; Zhao, L.; Kou, H.; Zhang, Y. Influence of pore size of porous titanium fabricated by vacuum diffusion bonding of titanium meshes on cell penetration and bone ingrowth. *Acta Biomater.* **2016**, *33*, 311−321.

(5) Lode, A.; Heiss, C.; Knapp, G.; Thomas, J.; Nies, B.; Gelinsky, M.; Schumacher, M. Strontium-modified premixed calcium phosphate cements for the therapy of osteoporotic bone defects. *Acta Biomater.* **2018**, *65*, 475−485.

(6) Kalluri, R.; LeBleu, V. S. The biology, function, and biomedical applications of exosomes. *Science* **2020**, *367*, No. eaau6977.

(7) Zhai, M.; Zhu, Y.; Yang, M.; Mao, C. Human Mesenchymal Stem Cell Derived Exosomes Enhance Cell-Free Bone Regeneration by Altering Their miRNAs Profiles. *Adv. Sci.* **2020**, *7*, No. 2001334.

(8) Iram, T.; Kern, F.; Kaur, A.; Myneni, S.; Morningstar, A. R.; Shin, H.; Garcia, M. A.; Yerra, L.; Palovics, R.; Yang, A. C.; Hahn, O.; Lu, N.; Shuken, S. R.; Haney, M. S.; Lehallier, B.; Iyer, M.; Luo, J.; Zetterberg, H.; Keller, A.; Zuchero, J. B.; Wyss-Coray, T. Young CSF restores oligodendrogenesis and memory in aged mice via Fgf17. *Nature* **2022**, *605*, 509−515.

(9) Ma, S.; W, S.; Ye, Y. X.; Ren, J.; Chen, R. Q.; Li, W.; Li, J. M.; Zhao, L. Y.; Zhao, Q.; Sun, G. Q.; Jing, Y.; Zuo, Y. S.; Xiong, M. Z.; Yang, Y. H.; Wang, Q. R.; Lei, J. H.; Sun, S. H.; Long, X.; Song, M. S.; Yu, S. Y.; Chan, P.; Wang, J. W.; Zhou, Q.; Belmonte, J. C. L.; Qu, J.; Zhang, W. Q.; Liu, G. H. Heterochronic parabiosis induces stem cell revitalization and systemic rejuvenation across aged tissues. *Cell Stem Cell* **2022**, *29*, 990−1005.e10.

(10) Geng, T.; Song, Z. Y.; Xing, J. X.; Wang, B. X.; Dai, S. P.; Xu, Z. S. Exosome Derived from Coronary Serum of Patients with Myocardial Infarction Promotes Angiogenesis Through the miRNA-143/IGF-IR Pathway. *Int. J. Nanomed.* **2020**, *15*, 2647−2658.

(11) Zhang, J.; Zhang, X. Ischaemic preconditioning-induced serum exosomes protect against myocardial ischaemia/reperfusion injury in rats by activating the PI3K/AKT signalling pathway. *Cell Biochem. Funct.* **2021**, *39*, 287−295.

(12) Cheng, A.; Krishnan, L.; Pradhan, P.; Weinstock, L. D.; Wood, L. B.; Roy, K.; Guldberg, R. E. Impaired bone healing following treatment of established nonunion correlates with serum cytokine expression. *J. Orthop. Res.* **2019**, *37*, 299−307.

(13) Working, Z. M.; Morris, E. R.; Chang, J. C.; Coghlan, R. F.; Johnstone, B.; Miclau, T., 3rd; Horton, W. A.; Bahney, C. S. A quantitative serum biomarker of circulating collagen X effectively correlates with endochondral fracture healing. *J. Orthop. Res.* **2021**, *39*, 53−62.

(14) Burska, A. N.; Giannoudis, P. V.; Tan, B. H.; Ilas, D.; Jones, E.; Ponchel, F. Dynamics of Early Signalling Events during Fracture Healing and Potential Serum Biomarkers of Fracture Non-Union in Humans. *J. Clin. Med.* **2020**, *9*, No. 492.

(15) Stewart, C. C.; O'Hara, N. N.; Orwig, D.; Hochberg, M. C.; Sprague, S.; Magaziner, J.; Slobogean, G. P. Serum 25(OH)D is associated with an altered bone turnover marker response after a hip fracture. *J. Orthop. Res.* **2019**, *37*, 535−540.

(16) Moghimi, S. M.; Hunter, A. C. Poloxamers and poloxamines in nanoparticle engineering and experimental medicine. *Trends Biotechnol.* **2000**, *18*, 412−420.

(17) Wang, X.; Wang, Y.; Gou, W.; Lu, Q.; Peng, J.; Lu, S. Role of mesenchymal stem cells in bone regeneration and fracture repair: a review. *Int. Orthop.* **2013**, *37*, 2491−2498.

(18) Kong, L.; Smith, W.; Hao, D. Overview of RAW264.7 for osteoclastogensis study: Phenotype and stimuli. *J. Cell. Mol. Med.* **2019**, *23*, 3077−3087.

(19) Tang, Y. T.; Huang, Y. Y.; Zheng, L.; Qin, S. H.; Xu, X. P.; An, T. X.; Xu, Y.; Wu, Y. S.; Hu, X. M.; Ping, B. H.; Wang, Q. Comparison of isolation methods of exosomes and exosomal RNA from cell culture medium and serum. *Int. J. Mol. Med.* **2017**, *40*, 834−844.

(20) Song, C.; Yang, X.; Lei, Y.; Zhang, Z.; Smith, W.; Yan, J.; Kong, L. Evaluation of efficacy on RANKL induced osteoclast from RAW264.7 cells. *J. Cell. Physiol.* **2019**, *234*, 11969−11975.

(21) Schott, N. G.; Friend, N. E.; Stegemann, J. P. Coupling Osteogenesis and Vasculogenesis in Engineered Orthopedic Tissues. *Tissue Eng., Part B* **2021**, *27*, 199−214.

(22) Liao, W.; Ning, Y.; Xu, H. J.; Zou, W. Z.; Hu, J.; Liu, X. Z.; Yang, Y.; Li, Z. H. BMSC-derived exosomes carrying microRNA-122-5p promote proliferation of osteoblasts in osteonecrosis of the femoral head. *Clin. Sci.* **2019**, *133*, 1955−1975.

(23) Chen, J.; Liu, M.; Luo, X.; Peng, L.; Zhao, Z.; He, C.; He, Y. Exosomal miRNA-486-5p derived from rheumatoid arthritis fibroblast-like synoviocytes induces osteoblast differentiation through the Tob1/BMP/Smad pathway. *Biomater. Sci.* **2020**, *8*, 3430−3442.

(24) Liu, J.; Wu, M.; Feng, G.; Li, R.; Wang, Y.; Jiao, J. Downregulation of LINC00707 promotes osteogenic differentiation of human bone marrowderived mesenchymal stem cells by regulating DKK1 via targeting miR103a3p. *Int. J. Mol. Med.* **2020**, *46*, 1029−1038.

(25) Xue, H.; Tu, Y.; Ma, T.; Wen, T.; Yang, T.; Xue, L.; Cai, M.; Wang, F.; Guan, M. miR-93-5p attenuates IL-1beta-induced chondrocyte apoptosis and cartilage degradation in osteoarthritis partially by targeting TCF4. *Bone* **2019**, *123*, 129−136.

(26) Yu, C.; Wu, D.; Zhao, C.; Wu, C. CircRNA TGFBR2/MiR-25-3p/TWIST1 axis regulates osteoblast differentiation of human aortic valve interstitial cells. *J. Bone Miner. Metab.* **2021**, *39*, 360−371.

(27) Tu, M.; Tang, J.; He, H.; Cheng, P.; Chen, C. MiR-142-5p promotes bone repair by maintaining osteoblast activity. *J. Bone Miner. Metab.* **2017**, *35*, 255−264.

(28) Mao, G.; Wu, P.; Zhang, Z.; Zhang, Z.; Liao, W.; Li, Y.; Kang, Y. MicroRNA-92a-3p Regulates Aggrecanase-1 and Aggrecanase-2 Expression in Chondrogenesis and IL-1beta-Induced Catabolism in Human Articular Chondrocytes. *Cell. Physiol. Biochem.* **2017**, *44*, 38−52.

(29) Liu, X.; Yan, C.; Deng, X.; Jia, J. Hsa_circularRNA_0079201 suppresses chondrocyte proliferation and endochondral ossification

by regulating the microRNA1403p/SMAD2 signaling pathway in idiopathic short stature. *Int. J. Mol. Med.* **2020**, *46*, 1993−2006.
(30) Wang, Q.; Li, Y.; Zhang, Y.; Ma, L.; Lin, L.; Meng, J.; Jiang, L.; Wang, L.; Zhou, P.; Zhang, Y. LncRNA MEG3 inhibited osteogenic differentiation of bone marrow mesenchymal stem cells from postmenopausal osteoporosis by targeting miR-133a-3p. *Biomed. Pharmacother.* **2017**, *89*, 1178−1186.
(31) Puzas, J. E. Commentary on ″Mandible exosomal ssc-mir-133b regulates tooth development in miniature swine via endogenous apoptosis″. *Bone Res.* **2018**, *6*, No. 29.
(32) Yang, C.; Jia, R.; Zuo, Q.; Zheng, Y.; Wu, Q.; Luo, B.; Lin, P.; Yin, L. microRNA-143-3p regulates odontogenic differentiation of human dental pulp stem cells through regulation of the osteoprotegerin-RANK ligand pathway by targeting RANK. *Exp. Physiol.* **2020**, *105*, 876−885.
(33) Wu, J. C.; Sun, J.; Xu, J. C.; Zhou, Z. Y.; Zhang, Y. F. Down-regulated microRNA-199a-3p enhances osteogenic differentiation of bone marrow mesenchymal stem cells by targeting Kdm3a in ovariectomized rats. *Biochem. J.* **2021**, *478*, 721−734.
(34) Zhang, G.; Zhou, Y.; Su, M.; Yang, X.; Zeng, B. Inhibition of microRNA-27b-3p relieves osteoarthritis pain via regulation of KDM4B-dependent DLX5. *Biofactors* **2020**, *46*, 788−802.
(35) Zhang, A.; Ma, S.; Yuan, L.; Wu, S.; Liu, S.; Wei, X.; Chen, L.; Ma, C.; Zhao, H. Knockout of miR-21-5p alleviates cartilage matrix degradation by targeting Gdf5 in temporomandibular joint osteoarthritis. *Bone Jt. Res.* **2020**, *9*, 689−700.
(36) Jin, Y. P.; Hu, Y. P.; Wu, X. S.; Wu, Y. S.; Ye, Y. Y.; Li, H. F.; Liu, Y. C.; Jiang, L.; Liu, F. T.; Zhang, Y. J.; Hao, Y. J.; Liu, X. Y.; Liu, Y. B. miR-143-3p targeting of ITGA6 suppresses tumour growth and angiogenesis by downregulating PLGF expression via the PI3K/AKT pathway in gallbladder carcinoma. *Cell Death Dis.* **2018**, *9*, No. 182.
(37) Li, Q.; Xu, Y.; Lv, K.; Wang, Y.; Zhong, Z.; Xiao, C.; Zhu, K.; Ni, C.; Wang, K.; Kong, M.; Li, X.; Fan, Y.; Zhang, F.; Chen, Q.; Li, Y.; Li, Q.; Liu, C.; Zhu, J.; Zhong, S.; Wang, J.; Chen, Y.; Zhao, J.; Zhu, D.; Wu, R.; Chen, J.; Zhu, W.; Yu, H.; Ardehali, R.; Zhang, J. J.; Wang, J.; Hu, X. Small extracellular vesicles containing miR-486-5p promote angiogenesis after myocardial infarction in mice and nonhuman primates. *Sci. Transl. Med.* **2021**, *13*, No. eabb0202.
(38) Lacerda, J. Z.; Ferreira, L. C.; Lopes, B. C.; Aristizabal-Pachon, A. F.; Bajgelman, M. C.; Borin, T. F.; Zuccari, D. Therapeutic Potential of Melatonin in the Regulation of MiR-148a-3p and Angiogenic Factors in Breast Cancer. *Microrna* **2019**, *8*, 237−247.
(39) Laganà, A.; Acunzo, M.; Romano, G.; Pulvirenti, A.; Veneziano, D.; Cascione, L.; Giugno, R.; Gasparini, P.; Shasha, D.; Ferro, A.; Croce, C. M. miR-Synth: a computational resource for the design of multi-site multi-target synthetic miRNAs. *Nucleic Acids Res.* **2014**, *42*, 5416−5425.
(40) Lu, Y.; Wen, H.; Huang, J.; Liao, P.; Liao, H.; Tu, J.; Zeng, Y. Extracellular vesicle-enclosed miR-486-5p mediates wound healing with adipose-derived stem cells by promoting angiogenesis. *J. Cell. Mol. Med.* **2020**, *24*, 9590−9604.
(41) Liang, L.; Zhao, L.; Zan, Y.; Zhu, Q.; Ren, J.; Zhao, X. MiR-93-5p enhances growth and angiogenesis capacity of HUVECs by down-regulating EPLIN. *Oncotarget* **2017**, *8*, 107033−107043.
(42) Yoshida, A.; Fujiwara, T.; Uotani, K.; Morita, T.; Kiyono, M.; Yokoo, S.; Hasei, J.; Nakata, E.; Kunisada, T.; Ozaki, T. Clinical and Functional Significance of Intracellular and Extracellular microRNA-25-3p in Osteosarcoma. *Acta Med. Okayama* **2018**, *72*, 165−174.
(43) Zhang, P.; Zhao, Q.; Gong, K.; Long, Y.; Zhang, J.; Li, Y.; Guo, X. Downregulation of miR-103a-3p Contributes to Endothelial Progenitor Cell Dysfunction in Deep Vein Thrombosis Through PTEN Targeting. *Ann. Vasc. Surg* **2020**, *64*, 339−346.
(44) Wu, W.; Shang, Y.; Dai, S.; Yu, C.; Wang, J. Downregulation of miR1425p inhibits human aortic smooth muscle cell proliferation and migration by targeting MKL2. *Mol. Med. Rep.* **2020**, *22*, 277−285.
(45) Yamada, N. O.; Heishima, K.; Akao, Y.; Senda, T. Extracellular Vesicles Containing MicroRNA-92a-3p Facilitate Partial Endothelial-Mesenchymal Transition and Angiogenesis in Endothelial Cells. *Int. J. Mol. Sci.* **2019**, *20*, No. 4406.
(46) Wang, L.; Liu, W. X.; Huang, X. G. MicroRNA-199a-3p inhibits angiogenesis by targeting the VEGF/PI3K/AKT signalling pathway in an in vitro model of diabetic retinopathy. *Exp. Mol. Pathol.* **2020**, *116*, No. 104488.
(47) Zhang, Z.; Guo, X.; Guo, X.; Yu, R.; Qian, M.; Wang, S.; Gao, X.; Qiu, W.; Guo, Q.; Xu, J.; Chen, Z.; Wang, H.; Qi, Y.; Zhao, R.; Xue, H.; Li, G. MicroRNA-29a-3p delivery via exosomes derived from engineered human mesenchymal stem cells exerts tumour suppressive effects by inhibiting migration and vasculogenic mimicry in glioma. *Aging* **2021**, *13*, 5055−5068.
(48) Zhou, S.; Liang, P.; Zhang, P.; Zhang, M.; Huang, X. The long noncoding RNA PDK1-AS/miR-125b-5p/VEGFA axis modulates human dermal microvascular endothelial cell and human umbilical vein endothelial cell angiogenesis after thermal injury. *J. Cell. Physiol.* **2021**, *236*, 3129−3142.
(49) Lehrskov, L. L.; Kjeldsen, S.; Lyngbaek, M. P.; Chirstensen, R. H.; Wedell-Neergaard, A. S.; Soderlund, L.; Jorgensen, N. R.; Krogh-Madsen, R.; Albrechtsen, N. J. W.; Ellingsgaard, H. Interleukin-6 May Not Affect Bone Resorption Marker CTX or Bone Formation Marker P1NP in Humans. *J. Endocr. Soc.* **2020**, *4*, No. bvaa093.
(50) Brady, J.; Hardy, B. M.; Yoshino, O.; Buxton, A.; Quail, A.; Balogh, Z. J. The effect of haemorrhagic shock and resuscitation on fracture healing in a rabbit model: an animal study. *Bone Jt. J.* **2018**, *100-B*, 1234−1240.
(51) Xuan, J. J.; Balakrishnan, P.; Oh, D. H.; Yeo, W. H.; Park, S. M.; Yong, C. S.; Choi, H. G. Rheological characterization and in vivo evaluation of thermosensitive poloxamer-based hydrogel for intramuscular injection of piroxicam. *Int. J. Pharm.* **2010**, *395*, 317−323.

https://doi.org/10.1021/acsami.3c00898
ACS Appl. Mater. Interfaces 2023, 15, 27486−27501